



# In situ construction of biocompatible Z-scheme $\alpha$ -Bi<sub>2</sub>O<sub>3</sub>/CuBi<sub>2</sub>O<sub>4</sub> heterojunction for NO removal under visible light

Qian Chen<sup>a</sup>, Huimin Long<sup>a</sup>, Meijuan Chen<sup>b</sup>, Yongfang Rao<sup>a,\*</sup>, Xinwei Li<sup>d,e</sup>, Yu Huang<sup>c,d,\*</sup>

<sup>a</sup> Department of Environmental Science and Engineering, Xi'an Jiaotong University, Xi'an 710049, PR China

<sup>b</sup> School of Human Settlements and Civil Engineering, Xi'an Jiaotong University, Xi'an 710049, PR China

<sup>c</sup> Key Laboratory of Aerosol Chemistry and Physics, Institute of Earth Environment, Chinese Academy of Sciences, Xi'an 710075, PR China

<sup>d</sup> State Key Lab of Loess and Quaternary Geology (SKLLQG), Institute of Earth Environment, Chinese Academy of Sciences, Xi'an, 710075, PR China

<sup>e</sup> Department of Civil and Environmental Engineering, The Hong Kong Polytechnic University, Hong Kong, PR China

## ARTICLE INFO

### Keywords:

In situ synthesis  
Z-scheme heterojunction  
Photocatalytic NO removal  
In situ DRIFTS  
Cytotoxicity

## ABSTRACT

The design of efficient, stable and biocompatible photocatalysts for air purification is still a challenge. In this work, we report a Z-scheme  $\alpha$ -Bi<sub>2</sub>O<sub>3</sub>/CuBi<sub>2</sub>O<sub>4</sub> composite with high-quality interfaces using an in situ synthesis method. The  $\alpha$ -Bi<sub>2</sub>O<sub>3</sub>/CuBi<sub>2</sub>O<sub>4</sub> displays significantly enhanced photocatalytic activity for NO removal (30 %) in comparison with  $\alpha$ -Bi<sub>2</sub>O<sub>3</sub> (17 %) under visible light irradiation. Based on characterizations, theoretical calculations and ESR tests, the Z-scheme migration mechanism of photoinduced electrons and holes on  $\alpha$ -Bi<sub>2</sub>O<sub>3</sub>/CuBi<sub>2</sub>O<sub>4</sub> heterojunction was proposed. The formation of intermediates and products was monitored by in situ DRIFTS. The NO adsorption and activation on  $\alpha$ -Bi<sub>2</sub>O<sub>3</sub>/CuBi<sub>2</sub>O<sub>4</sub> surface are more favorable than that on  $\alpha$ -Bi<sub>2</sub>O<sub>3</sub> surface. The  $\alpha$ -Bi<sub>2</sub>O<sub>3</sub>/CuBi<sub>2</sub>O<sub>4</sub> also shows high selectivity for the conversion of NO to NO<sub>2</sub>. Moreover, the cytotoxicity of  $\alpha$ -Bi<sub>2</sub>O<sub>3</sub>/CuBi<sub>2</sub>O<sub>4</sub> exposed to human alveolar epithelial cell has been evaluated for its potential application in air purification. This work provides a new perspective regarding the design of Z-scheme heterojunctions by an in situ method and a promising photocatalyst suitable for air pollution control.

## 1. Introduction

Nitrogen oxides (NO<sub>x</sub>) are not only one of the important precursors for the formation of secondary organic aerosols and heavy haze [1], but also can induce multifarious diseases in humans [2]. Hence, there is an urgent need to develop effective and economic measures to reduce NO<sub>x</sub> concentration in the atmosphere. The high concentration NO<sub>x</sub> emitted by fossil fuel combustion can be reduced through conventional techniques (selective catalytic reduction and adsorption) [3,4]. These techniques with high cost are not suitable for the removal of NO<sub>x</sub> at part-per-billion (ppb) levels. Photocatalysis, as a promising and green technology, can utilize clean solar energy to achieve air purification [5,6]. The major obstacles for the practical application of photocatalysis in NO removal include low utilization of solar energy, easy recombination of photogenerated carriers, weak redox capacity and the generation of toxic by-products [7–9]. Hence, the rational development and design of satisfactory photocatalysts is essential to solve these problems.

Bismuth-based catalysts are considered to be ideal candidates for photocatalytic decontamination due to strong visible light adsorption

[10–12]. Bismuth trioxide (Bi<sub>2</sub>O<sub>3</sub>) has four main crystalline phases  $\alpha$ ,  $\beta$ ,  $\gamma$  and  $\delta$ , with band gap ranging from 2.5 eV to 2.8 eV [13]. Thereinto, monoclinic  $\alpha$ -Bi<sub>2</sub>O<sub>3</sub> has been widely studied due to its stability and visible light response [13,14]. However, the photocatalytic activity of  $\alpha$ -Bi<sub>2</sub>O<sub>3</sub> is restrained owing to the rapid recombination of photoinduced electrons and holes [14–16].

Constructing heterojunction by coupling two or more semiconductors is one of the most effective and feasible strategies to tackle this problem. However, the conventional Type-II heterojunction cannot obtain both high carrier separation efficiency and strong redox capability at the same time. Recently, various direct Z-scheme heterojunction systems based on two semiconductors with matched energy levels have been extensively studied [17–19]. These heterojunction systems favor the separation of carriers while retaining strong redox capability. The electrons and holes with appropriate potentials staying on two different semiconductors participate in photocatalytic reactions [20–22]. Nonetheless, it is difficult to prepare homogeneous heterojunction structure with low interface transmission resistance of carriers [23]. Previous studies have shown that the in situ strategy can realize uniform distribution of one component over the other and the intimate

\* Corresponding authors.

E-mail addresses: [yf Rao@mail.xjtu.edu.cn](mailto:yf Rao@mail.xjtu.edu.cn) (Y. Rao), [huangyu@ieecas.cn](mailto:huangyu@ieecas.cn) (Y. Huang).

<https://doi.org/10.1016/j.apcatb.2020.119008>

Received 17 January 2020; Received in revised form 9 April 2020; Accepted 11 April 2020

Available online 18 April 2020

0926-3373/© 2020 Elsevier B.V. All rights reserved.

interfaces, which is favorable for the carrier transport and separation [24,25].

CuBi<sub>2</sub>O<sub>4</sub>, as a novel p-type semiconductor whose band gap ranges from 1.4 eV to 1.8 eV, has received extensive attention in the field of photocatalysis. CuBi<sub>2</sub>O<sub>4</sub> can utilize the adequate visible light and its conduction band minimum has a potential more negative than the reduction potential of O<sub>2</sub>/O<sup>•-</sup> 2 (-0.33 eV vs NHE) [26–28]. However, pure CuBi<sub>2</sub>O<sub>4</sub> exhibits poor photocatalytic activity due to the rapid recombination of the photogenerated carriers. A variety of CuBi<sub>2</sub>O<sub>4</sub> heterojunctions, such as CuBi<sub>2</sub>O<sub>4</sub>/Bi<sub>2</sub>WO<sub>6</sub> [29,30] and CuBi<sub>2</sub>O<sub>4</sub>/Ag<sub>3</sub>PO<sub>4</sub> [31], have been constructed to improve the carrier separation efficiency. However, these Z-scheme heterojunctions were not prepared by an in situ synthesis method. And they were applied to photocatalytic removal of water pollutants.

Considering the practical application of photocatalysts, the biocompatibility cannot be ignored. N. B. Hartmann et al. reported that TiO<sub>2</sub> nanoparticles inhibited the growth of green algae and the inhibiting effect exhibited a dose-response relationship [32]. The intracellular ROS in normal skin cells was induced by ZnO nanoparticles, leading to cell death [33]. Therefore, the good biocompatibility of the photocatalysts is one of major concerns for its practical application.

In this study, we used an in situ synthesis method to fabricate a Z-scheme  $\alpha$ -Bi<sub>2</sub>O<sub>3</sub>/CuBi<sub>2</sub>O<sub>4</sub> heterojunction with high-quality interfacial contact and strong redox ability for the first time. The photocatalytic performance of  $\alpha$ -Bi<sub>2</sub>O<sub>3</sub>/CuBi<sub>2</sub>O<sub>4</sub> was evaluated in terms of NO removal efficiency and the generation of toxic intermediates. The separation and migration of charges were analyzed via theoretical calculations and characterizations. The reaction pathways of photocatalytic NO oxidation were proposed on the basis of in situ DRIFTS measurement. In addition, the biocompatibility of photocatalysts was also tested through in vitro cytotoxicity experiments.

## 2. Experimental section

### 2.1. Synthesis of $\alpha$ -Bi<sub>2</sub>O<sub>3</sub>/CuBi<sub>2</sub>O<sub>4</sub> composites

All reagents are analytical grade and used directly without further purification. The  $\alpha$ -Bi<sub>2</sub>O<sub>3</sub>/CuBi<sub>2</sub>O<sub>4</sub> composites were prepared by solvothermal reaction and calcination for the first time. Bismuth nitrate and copper nitrate were respectively dispersed in the same volume of methanol and deionized water at a molar ratio of 2:1. Then, the two solutions were mixed and stirred for 20 min. A predetermined volume of DMF (N, N-Dimethylformamide) solution containing a certain amount of H<sub>3</sub>BTC (1,3,5-Benzenetricarboxylic acid) was added into the above mixed solution slowly under continuous stirring. After 1 h, the obtained suspension was transferred into a 50 mL Teflon lining autoclave and heated at 120 °C for 24 h. When the autoclave was cooled down to room temperature naturally, the resulting precipitate was collected by centrifugation, and washed thoroughly with absolute ethanol for several times, dried at 80 °C for 24 h. The synthesized precursor was labeled as Bi/Cu-BTC. Then, Bi/Cu-BTC precursor was calcined at different temperatures (400 °C–700 °C) for 3 h. The acquired  $\alpha$ -Bi<sub>2</sub>O<sub>3</sub> and CuBi<sub>2</sub>O<sub>4</sub> composites were recorded as BO/CBO-T, where T represents the calcination temperature. While the thermal decomposition temperature was 800 °C, a pure CuBi<sub>2</sub>O<sub>4</sub> was obtained, which was named as CBO-800. Pure  $\alpha$ -Bi<sub>2</sub>O<sub>3</sub> was synthesized using the same solvothermal process without copper source, and then calcined at 400 °C, marked as BO-400.

The characterization methods, photocatalytic activity evaluation, photoelectrochemical measurements and theoretical calculation are detailed in the supporting information.

### 2.2. In Situ DRIFTS investigation of the NO adsorption and oxidation

In situ DRIFTS measurement was conducted on a VERTEX 70 FT-IR spectrometer (Bruker, Germany) (Fig. S2). The samples were pretreated

in He for 1 h at 100 °C to remove impurities from the catalyst surface and then cooled to room temperature (25 °C). The IR spectrum at this time was recorded as the background. Then, the gas mixture of NO + O<sub>2</sub> (30 mL min<sup>-1</sup> NO and 30 mL min<sup>-1</sup> O<sub>2</sub>) was injected into the reaction chamber. In the dark, the adsorption of NO on catalyst was carried out for 30 min. Then, the light source ( $\geq$  420 nm) was introduced to start the photocatalytic reaction for 30 min.

### 2.3. Cytotoxicity and Intracellular reactive oxygen species (ROS) assays

The A549 cells, as a type II human alveolar epithelial cell, were used to evaluate the cytotoxicity of BO-400 and BO/CBO-400 through CCK-8 assay as described by Li et al. [34] The detailed procedures regarding cell culture, preparation of particle suspensions, cell counting and intracellular ROS assays are described in the supporting information.

## 3. Results and discussion

### 3.1. Phase structure, Chemical compositions and morphologies

Thermogravimetric analysis (TGA) was performed to determine the calcination temperature at which the precursor (Bi/Cu-BTC) decomposes to form metal oxides. The results show that metal oxides may begin to be generated at 400 °C (Fig. S3a). In addition, thermogravimetric analysis of BO/CBO-400 proves that there is no carbon in the sample (Fig. S3b).

The phase structure of as-synthesized photocatalysts was analyzed by X-ray diffraction. All the diffraction peaks of BO-400 are consistent with the characteristic peaks of pure monoclinic  $\alpha$ -Bi<sub>2</sub>O<sub>3</sub> (JCPDS No. 71-2274) (Fig. S4). The precursor (Bi/Cu-BTC) was annealed at 400 °C, a composite of  $\alpha$ -Bi<sub>2</sub>O<sub>3</sub> and CuBi<sub>2</sub>O<sub>4</sub> was generated without other peaks. The intensity of diffraction peak of BO-400 (1(-)21) plane weakens and the (012) plane of BO-400 is gradually converted to the (211) plane of CBO-800 with the increase of the calcination temperature (see Fig. 1a). The diffraction peaks of (200), (220) and (002) planes of CBO-800 are also found (Fig. 1a). At 800 °C, the diffraction peaks are indexed to the pure tetragonal CuBi<sub>2</sub>O<sub>4</sub> (JCPDS No. 71-1774) without any  $\alpha$ -Bi<sub>2</sub>O<sub>3</sub> peak being detected. This phenomenon is probably attributed to the small radius of copper and the high mobility of ions at high temperatures, which facilitates the migration and diffusion of copper ions into  $\alpha$ -Bi<sub>2</sub>O<sub>3</sub> to form another crystal structure CuBi<sub>2</sub>O<sub>4</sub> [27,35]. Moreover, studies have shown that the formation of a composite  $\alpha$ -Bi<sub>2</sub>O<sub>3</sub> and CuBi<sub>2</sub>O<sub>4</sub> can be observed with the temperature lower than 730 °C and pure CuBi<sub>2</sub>O<sub>4</sub> were generated at the temperature above 770 °C [36]. The above results demonstrate that the BO/CBO heterojunction were successfully constructed by in situ synthesis. Fig. 1b shows the crystal structure model of the BO/CBO heterojunction.

The surface chemical compositions and states of the prepared BO/CBO-400, BO-400 and CBO-800 were further explored by XPS. The appearance of Cu element is observed in XPS full spectrum of the BO/CBO-400, which further proves the existence of CBO (Fig. S5a). The two symmetrical characteristic peaks at 164.0 eV and 158.7 eV in BO-400 correspond to Bi 4f<sub>5/2</sub> and Bi 4f<sub>7/2</sub> of Bi<sup>3+</sup>, whereas the same two peaks of BO/CBO-400 shift to lower binding energy (Fig. S5b) [14,37]. As shown in Fig. 1c, the two distinct sharp peaks at 934.3 eV and 954.3 eV are the binding energies of Cu 2p<sub>3/2</sub> and Cu 2p<sub>1/2</sub> with a difference of approximately 20 eV between them for spin-orbit splitting, which is consistent with the characteristic peaks of Cu<sup>2+</sup> [31,38]. The Cu 2p peaks in BO/CBO-400 shift to lower binding energy by approximately 0.1 eV compared to pure CBO-800, indicating that the formation of the BO/CBO-400 heterojunction results in the electrons density variation between two semiconductors [22]. Meanwhile, the vicinity of Cu 2p<sub>3/2</sub> and Cu 2p<sub>1/2</sub> are accompanied by two shake-up satellite peaks, which are characteristic of Cu<sup>2+</sup> [39]. In the O 1s spectrum of BO-400 (Fig. 1d), the peaks at 529.4 eV and 530.8 eV correspond to the lattice

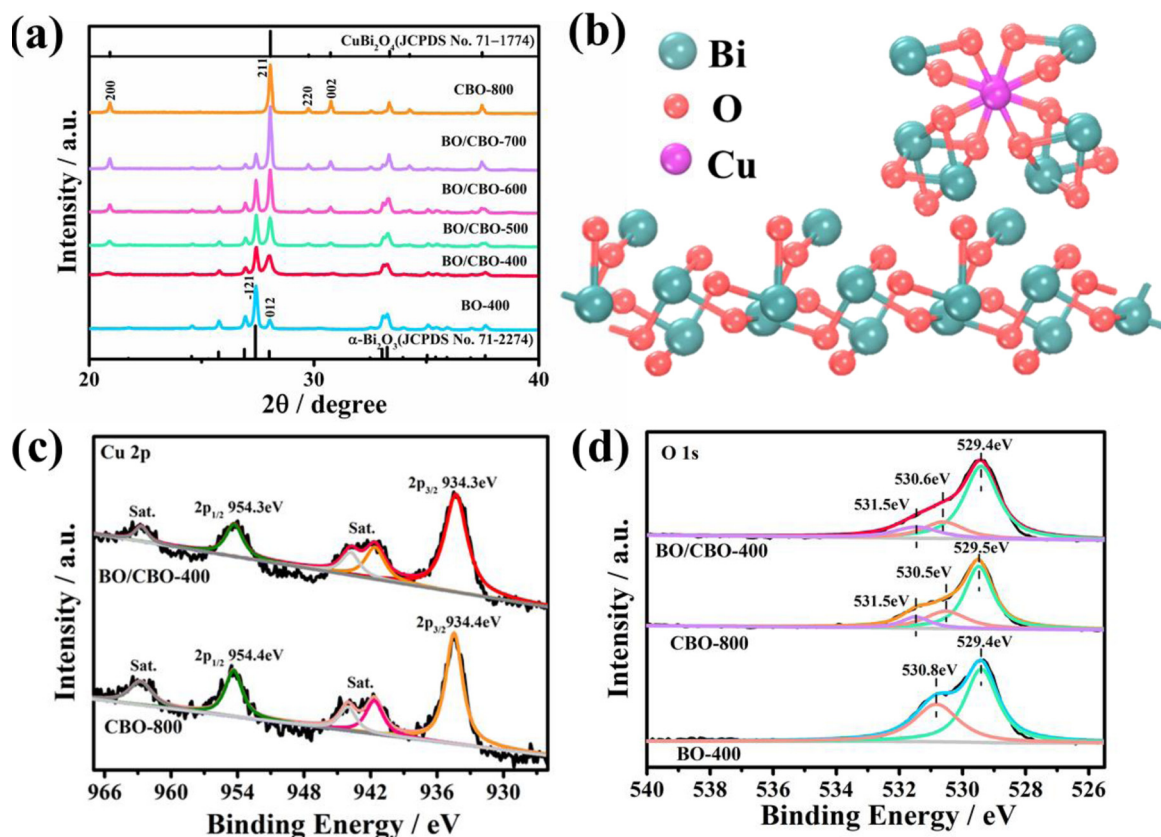


Fig. 1. The XRD patterns ( $2\theta = 20^\circ$ – $40^\circ$  enlargement) of all samples (a); The structural model of BO/CBO heterojunction (b); The high-resolution XPS spectra of Cu 2p (c) and O 1s (d) of as-prepared samples.

oxygen species and surface adsorbed water. The O 1s spectrum of BO/CBO-400 could be deconvoluted into three characteristic peaks. The new peak at 531.5 eV is classified as the adsorbed hydroxyl group [40,41]. It is confirmed by XPS analysis that  $\text{CuBi}_2\text{O}_4$  was successfully formed on the surface of  $\alpha$ - $\text{Bi}_2\text{O}_3$ .

The microscopic morphologies of the samples were observed via SEM. As illustrated in Fig. 2a, the BO-400 exhibits a non-uniform rod-like structure with approximately 5–10  $\mu\text{m}$  in length and 200 nm–3  $\mu\text{m}$  in diameter. The morphology of BO/CBO-400 is similar to that of BO-

400 (Fig. 2b), but there are small nanoparticles on the surface of rod-like  $\alpha$ - $\text{Bi}_2\text{O}_3$  (Fig. 2b inset). Since the synthesis conditions of BO/CBO-400 are consistent with those of BO-400 except for the addition of copper, it is reasonable to speculate that these nanoparticles are  $\text{CuBi}_2\text{O}_4$ . Meanwhile, the elemental mapping images (Fig. 2g) indicate that Bi (blue), Cu (green), O (magenta) elements are evenly dispersed over the entire rod-like area of BO/CBO-400. The rod-like structure gradually disappeared with calcination temperatures increasing from 500  $^\circ\text{C}$  to 700  $^\circ\text{C}$  (Fig. 2c–e). Fig. 2f shows that the CBO-800 exhibits an irregular polygonal block. In addition, the EDX analysis of the BO/CBO composites confirms that the relative contents of  $\alpha$ - $\text{Bi}_2\text{O}_3$  and  $\text{CuBi}_2\text{O}_4$  varied with the calcination temperatures (Table S1) [42].

TEM and HRTEM were utilized to further investigate the morphological structure and crystal characteristics of the representative samples. As shown in Fig. 3a, BO-400 reveals a solid rod-like appearance. The corresponding HRTEM image (Fig. 3c) displays legible lattice fringes, and the lattice spacings of 0.405 nm and 0.324 nm are consistent with the (020) plane and (120) plane d-spacing value of  $\alpha$ - $\text{Bi}_2\text{O}_3$  (JCPDS No. 71-2274), respectively [16]. Fig. 3b presents that small nanoparticles were formed and adhered to the  $\alpha$ - $\text{Bi}_2\text{O}_3$  rods, which agrees with the SEM results. The edges of the rod-like composite were observed at high magnification (Fig. 3d), which exhibits two distinct lattice fringes. The lattice spacings of 0.405 nm and 0.324 nm correspond to the (020) and (120) crystal planes of  $\alpha$ - $\text{Bi}_2\text{O}_3$ , whereas the lattice spacing of 0.315 nm is indexed to the (211) crystal plane of  $\text{CuBi}_2\text{O}_4$  (JCPDS No. 71-1774) [29]. The HRTEM image of the BO/CBO-400 composite evidences the heterojunction interface with close contact, which favors the transmission of photogenerated carriers at the interface.

NO removal efficiency was used to evaluate the photocatalytic activities of the synthesized samples under visible light ( $\lambda \geq 420$  nm). Fig. 4a shows the change in NO concentration with illumination time.

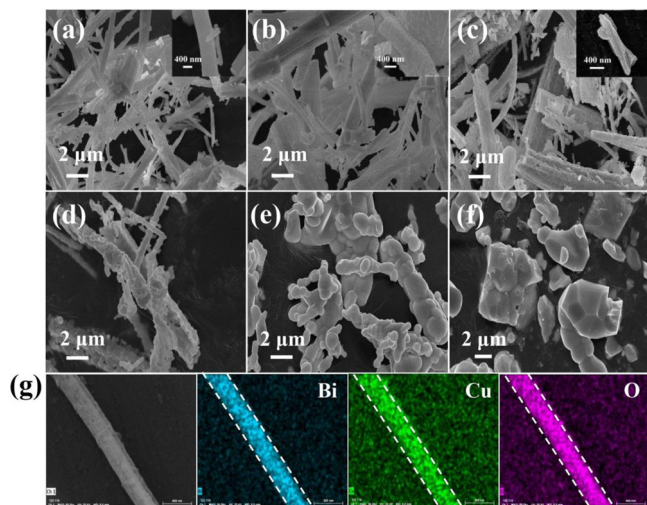


Fig. 2. SEM images of low resolutions and high resolutions (inset) of BO-400 (a), BO/CBO-400 (b) and BO/CBO-500 (c); SEM images of BO/CBO-600 (d), BO/CBO-700 (e) and CBO-800 (f) at low resolutions; (g) elemental mapping of Bi, Cu and O in BO/CBO-400.



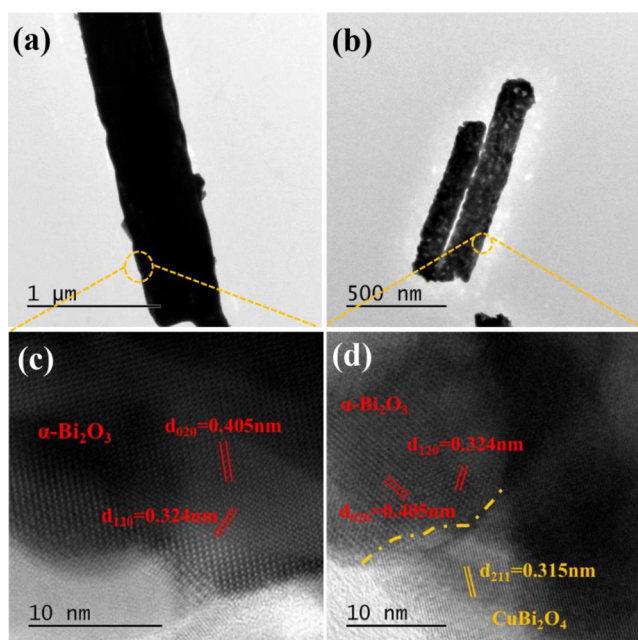


Fig. 3. TEM and HRTEM images of BO-400 (a, c) and BO/CBO-400 (b, d).

The NO removal efficiency of 17 % was achieved over BO-400 under 30 min visible light irradiation. CBO-800 exhibits very low photocatalytic activity. This is because its narrow band gap results in the rapid recombination of photoexcited electrons and holes. Nevertheless, compared to BO-400, BO/CBO-400 exhibits much better photocatalytic activity in terms of NO removal efficiency (30 %) under visible light irradiation of 30 min. The effect of calcination temperature on the photocatalytic activity of the composites is shown in Fig. S6, displaying that BO/CBO-400 has the maximum removal efficiency (30 %) among all BO/CBO composites. To demonstrate the effect of high-quality interfaces by in situ synthesis, a mechanically-mixed sample was prepared, containing two pure phases in similar composition to BO/CBO-400. The photocatalytic performance of the mechanically-mixed sample (15 %) is worse than that of BO/CBO-400 heterojunction (30 %), indicating that intimate interface contact is beneficial to improve the photocatalytic activity of composites.

NO<sub>2</sub>, as a noxious by-product, was also monitored online (Fig. 4b). The NO<sub>2</sub> concentration generated over BO/CBO-400 is significantly lower than that over BO-400, suggesting that the BO/CBO-400 heterojunction effectively inhibits the production of NO<sub>2</sub>. The NO<sub>2</sub> selectivity of all samples was summarized in Fig. S7. BO/CBO-400 displays much lower conversion (6.69 %) of NO to NO<sub>2</sub> than BO-400 (32.25 %). After photocatalytic reaction, the accumulated products on the photocatalysts surface were collected with deionized water and detected (Fig. S8). The results indicate that the amount of produced NO<sub>3</sub> and NO<sub>2</sub> over BO/CBO-400 is 280.5 and 44 μg g<sup>-1</sup>, respectively,

while that over BO-400 is 152.5 and 23.5 μg g<sup>-1</sup>.

In order to further explore the reproducibility and stability of the photocatalyst, the cycle experiment of BO/CBO-400 was conducted under the same conditions (Fig. S9a). The photocatalytic activity of BO/CBO-400 decreased slightly as cycling times increased, but its activity was restored to the original level after BO/CBO-400 being washed with deionized water. The used BO/CBO-400 was collected and tested for XRD, demonstrating that the crystal structure of the used BO/CBO-400 is consistent with that of its fresh sample (Fig. S9b).

### 3.2. Textural, optical properties and charge separation efficiency

The nitrogen adsorption-desorption isotherms were performed to investigate the specific surface areas of the samples, as shown in Fig. S10a. The specific surface area of BO/CBO-400, BO-400 and CBO-800 is 4.97, 2.23 and 1.85 m<sup>2</sup> g<sup>-1</sup>. The BO/CBO-400 displays type-IV isotherm with a hysteresis loop, suggesting the existence of mesopores [24]. As illustrated in Fig. S10b, the peak around 75 nm in BO-400 confirms the existence of macropores. The CBO-800 isotherm and pore size distribution pattern indicate that almost no pore structure was formed in CBO-800 [43], which may be due to the sample being sintered at high temperature. The abundant pore structure of BO/CBO-400 composite provides enough surface active sites for photocatalytic reactions.

The optical properties and band gap structure of the prepared samples were investigated using UV-vis diffuse reflectance spectra. As illustrated in Fig. 5a, CBO-800 can strongly absorb the visible light in the whole region, while BO-400 shows weak visible light absorption (edge at 450 nm). The light absorption range of BO/CBO-400 is similar to that of pure CBO-800, indicating that the formed CBO nanoparticles enhance the absorption of the composite in the visible region due to the narrow band gap of CuBi<sub>2</sub>O<sub>4</sub>. The band gap energies ( $E_g$ ) of BO-400 and CBO-800 are calculated by the following formula [24]:

$$\alpha h\nu = A(h\nu - E_g)^{n/2} \quad (1)$$

where  $\alpha$ ,  $h$ ,  $\nu$  and  $A$  are the molar absorption coefficient, the Planck constant, the incident photo frequency and the proportionality constant, respectively, and  $n$  depends on the semiconductor charge transition properties. The  $E_g$  of BO-400 and CBO-800 are estimated to be 2.65 eV and 1.60 eV from  $(\alpha h\nu)^{1/2}$  vs  $h\nu$  plot and  $(\alpha h\nu)^2$  vs  $h\nu$  plot, respectively (Fig. S11) [31,41]. The valence band position and conduction band position of the photocatalyst are important factors to determine the generation of reactive oxygen species. The valence band potentials ( $E_{VB}$ ) of the prepared samples were determined by XPS valence band spectra (Fig. S12). The valence band potentials ( $E_{VB}$ ) of BO-400 and CBO-800 are 2.81 eV and 0.83 eV, respectively. Thus, the conduction band potentials ( $E_{CB}$ ) of BO-400 and CBO-800 are calculated to be 0.16 eV and -0.77 eV, respectively.

To further understand the cause of the increase in photocatalytic activity, photoelectrochemical testing was utilized to probe the divorcement of photogenerated carriers. As shown in Fig. 5b, the photocurrent generated over the BO/CBO-400 heterojunction (2.0 μA

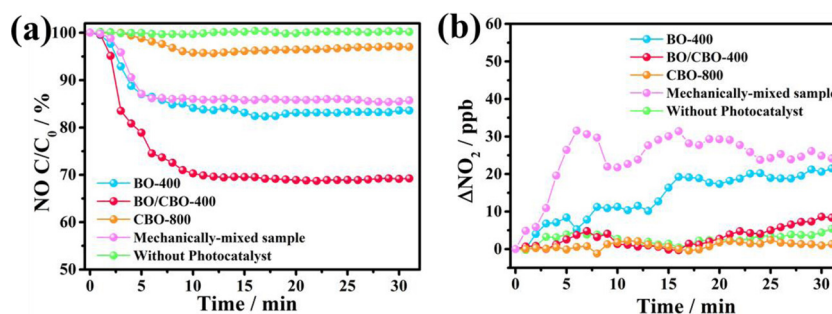


Fig. 4. Photocatalytic activities for NO removal (a) and the generation of NO<sub>2</sub> (b) of as-prepared samples.

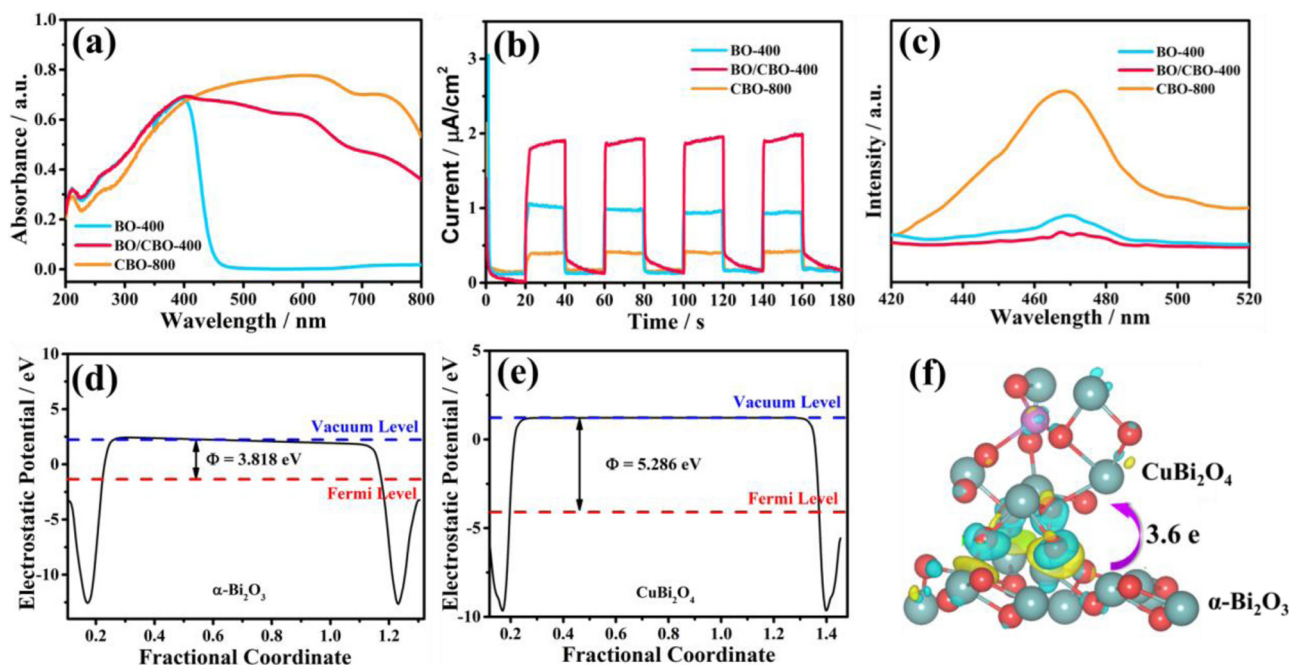


Fig. 5. UV-vis DRS spectra (a), transient photocurrent responses (b) and photoluminescence spectra (c) of BO-400, BO/CBO-400 and CBO-800 samples; The work functions of (d)  $\alpha$ -Bi<sub>2</sub>O<sub>3</sub> (001) surface and (e) CuBi<sub>2</sub>O<sub>4</sub> (100) surface; (f) the charge difference distribution of the BO/CBO interfacial structure (the charge accumulation region is in blue and the charge depletion region is in yellow) (For interpretation of the references to colour in this figure legend, the reader is referred to the web version of this article).

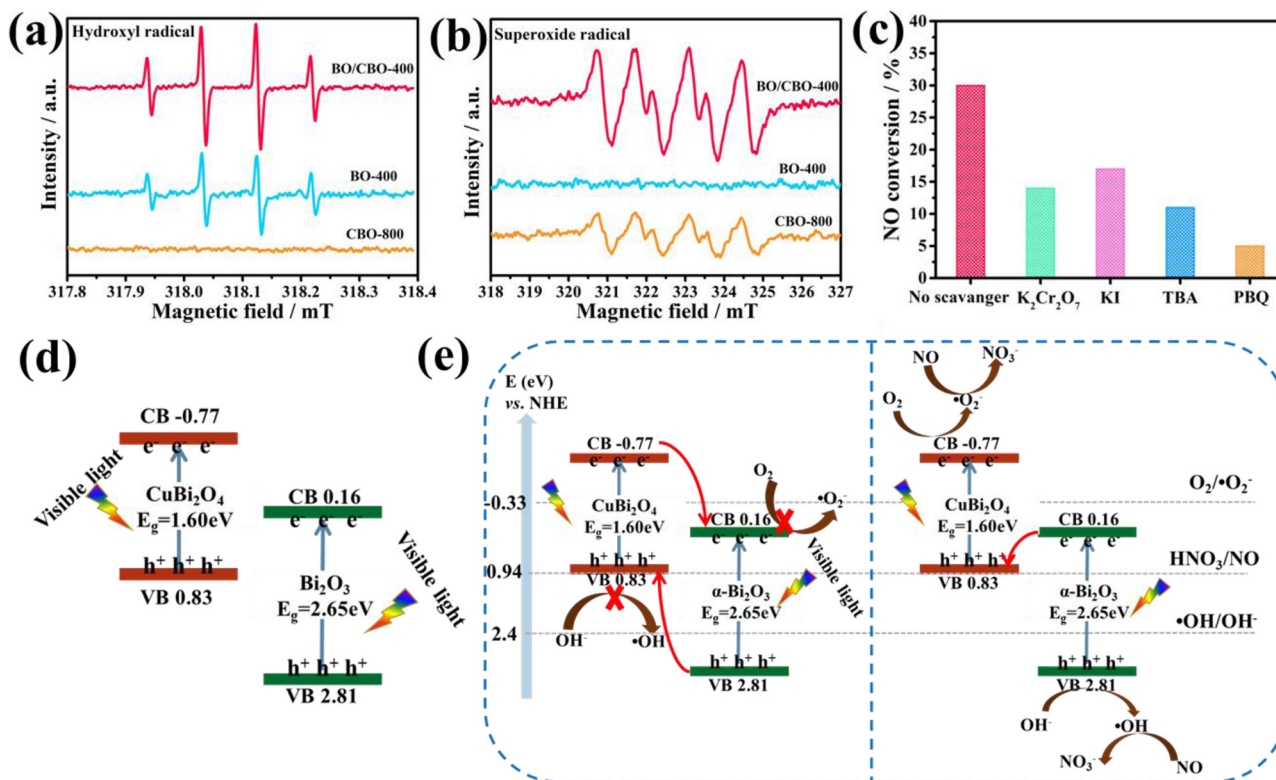


Fig. 6. ESR spectra of DMPO- $\cdot$ OH (a) and DMPO- $\text{O}_2^{\cdot-}$  (b) of BO-400, BO/CBO-400 and CBO-800 under 5 min visible light irradiation; (c) NO removal efficiency over BO/CBO-400 in the presence of different scavengers; The schematic diagram of energy structure (d) and charge transfer (e) of BO/CBO-400 heterojunction.

$\text{cm}^{-2}$ ) is 4 and 2 times that of CBO-800 ( $0.5 \mu\text{A cm}^{-2}$ ) and BO-400 ( $1.0 \mu\text{A cm}^{-2}$ ), respectively. This result implies that the constructed BO/CBO-400 heterojunction significantly accelerates the separation of photoinduced electron and hole pairs [37,44]. In the EIS Nyquist plots (Fig. S13a), the arc radius of BO/CBO-400 is remarkably smaller than

that of the other two single components, implying that the charge transfer resistance is reduced. The similar results were also authenticated by the photoluminescence (PL) emission spectra (Fig. 5c). The BO/CBO-400 displays the lowest emission intensity compared with BO-400 and CBO-800, indicating that the recombination of photogenerated

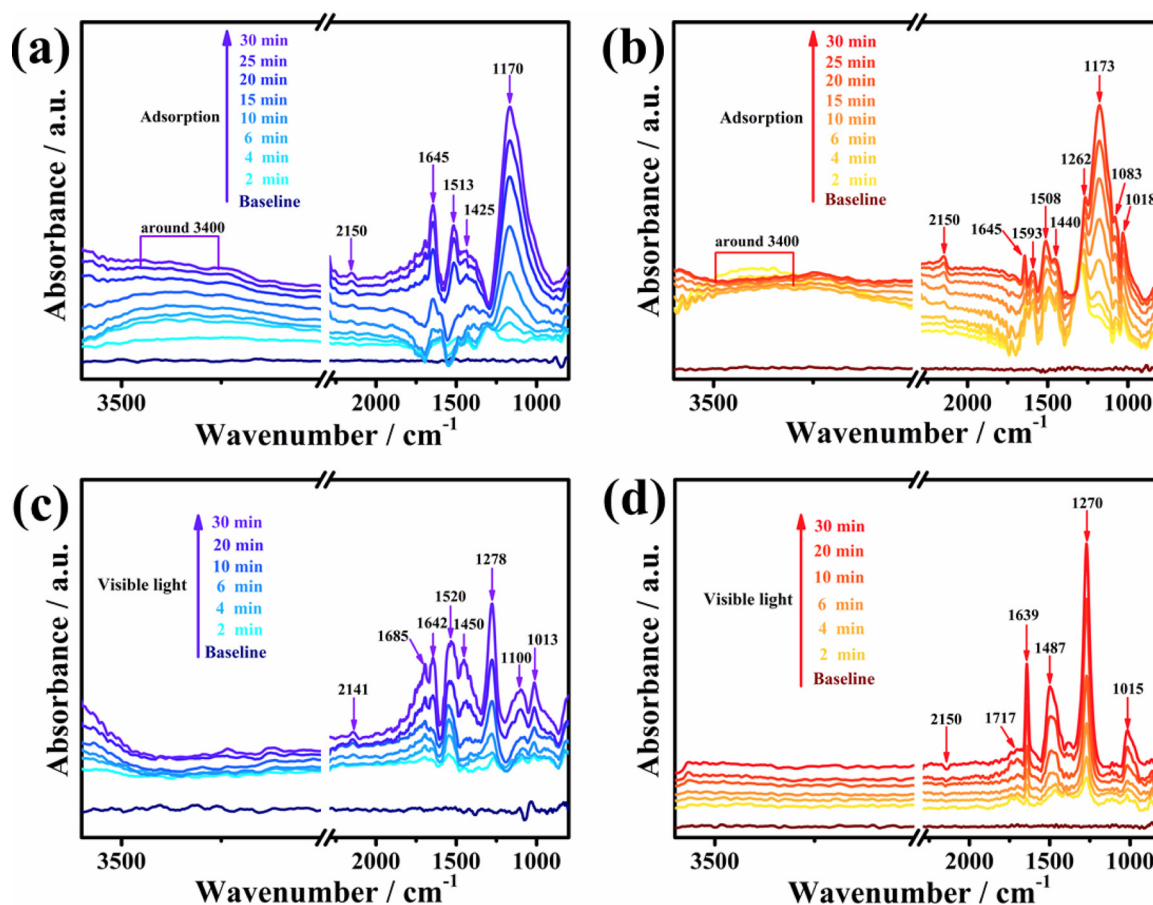


Fig. 7. In situ DRIFTS spectra of the NO adsorption and photocatalytic NO oxidation of BO-400 (a,c) and BO/CBO-400 (b,d).

carriers has been adequately restrained over BO/CBO-400.

The theoretical calculation was used to explore the interaction and charge transfer direction at the BO/CBO interface. The surface work functions of  $\alpha$ - $\text{Bi}_2\text{O}_3$  and  $\text{CuBi}_2\text{O}_4$  are calculated to be 3.818 eV and 5.286 eV, respectively (Fig. 5d and 5e). The difference in work function indicates the existence of charge migration at the interface of  $\alpha$ - $\text{Bi}_2\text{O}_3$  and  $\text{CuBi}_2\text{O}_4$ . The work function of  $\alpha$ - $\text{Bi}_2\text{O}_3$  is obviously smaller than that of  $\text{CuBi}_2\text{O}_4$ . When the BO/CBO heterojunction is constructed, electrons will migrate from  $\alpha$ - $\text{Bi}_2\text{O}_3$  to  $\text{CuBi}_2\text{O}_4$  until the Fermi levels of the two reach equilibrium. This charge migration results in the formation of a built-in electric field. Therefore, the photoinduced electrons on the  $\alpha$ - $\text{Bi}_2\text{O}_3$  will transfer to the  $\text{CuBi}_2\text{O}_4$  during the photocatalytic reaction, thereby effectively inhibiting the recombination of photo-generated carriers [45,46]. In addition, the electron localization function (ELF) indicates the strong covalent interaction between  $\alpha$ - $\text{Bi}_2\text{O}_3$  and  $\text{CuBi}_2\text{O}_4$  (Fig. S13b). The charge difference distribution of the optimal BO/CBO geometry was also calculated, as shown in Fig. 5f. The total charges ( $\Delta q$ ) value of CBO calculated through the Bader method is -3.6 e, where the negative value of  $\Delta q$  represents the accumulation of electrons. Therefore, the result shows that approximately 3.6 free electrons migrate from  $\alpha$ - $\text{Bi}_2\text{O}_3$  to  $\text{CuBi}_2\text{O}_4$  [10,47]. Based on the experimental results and theoretical calculations, we can conclude that the interaction and charge transport at the BO/CBO interface are conducive to the spatial separation of photogenerated electrons and holes, thereby improving the photocatalytic performance.

### 3.3. Reactive oxygen species and charge transfer mechanism

To ascertain reactive oxygen species (ROS) in the photocatalytic systems, ESR measurements were performed under visible light. As indicated in Fig. 6a, the characteristic signals of DMPO-O $\cdot$ H are

observed over BO/CBO-400 and BO-400, and the former signal is stronger than the latter after being irradiated for the same time [48]. However, the DMPO-O $\cdot$ H signal was not detected for CBO-800 due to the weak oxidation potential (0.83 eV vs NHE) of the photogenerated holes. Fig. 6b shows that the DMPO-O $\cdot$ -2 signal detected over BO/CBO-400 is significantly stronger than that of CBO-800 [23]. In general, the main reactive oxygen species are  $\cdot$ OH and O $\cdot$ -2 for BO/CBO-400. At the same time, trapping experiments were conducted to illustrate the active species involved in the reaction (Fig. 6c). The photocatalytic activity was substantially inhibited after  $\cdot$ O $\cdot$ -2 and O $\cdot$ H being captured, indicating that  $\cdot$ OH and O $\cdot$ -2 play an important role in the photocatalytic NO oxidation.

Based on the band structure of BO/CBO-400 (Fig. 6d) and ROS identification, the Z-scheme mechanism for the charge transfer over the BO/CBO-400 heterojunction is proposed. The CB edge of CBO-800 is located at -0.77 eV, more negative than the redox potential of  $\text{O}_2/\text{O}\cdot^-$ 2 (-0.33 eV vs NHE) [29]. Therefore,  $\text{O}_2$  can be reduced by the electrons on the CB of CBO-800 to form O $\cdot$ -2. Since the VB edge (0.83 eV) of CBO-800 is below the potential of  $\text{OH}^-/\text{O}\cdot\text{H}$  (2.4 eV vs NHE) [44], photoexcited holes cannot oxidize  $\text{OH}^-$  to generate O $\cdot$ H. There is a different scenario for BO-400. The VB holes of BO-400 are at 2.81 eV, which can generate O $\cdot$ H to oxidize NO, but the electrons on the CB cannot directly reduce  $\text{O}_2$ .

According to the above results, the photoinduced  $\text{e}^-$  on the CB of CBO-800 will not be transferred to the CB of BO-400. The photoinduced  $\text{h}^+$  on the VB of BO-400 cannot be migrated to CBO-800. After BO-400 and CBO-800 are excited by visible light, photogenerated  $\text{e}^-$  on the CB of BO-400 and photogenerated  $\text{h}^+$  on the VB of CBO-800 are more likely to recombine because of electrostatic interaction. The electrons with higher reducing ability and holes with stronger oxidizing ability stay on the CB of CBO-800 and the VB of BO-400 to participate in the



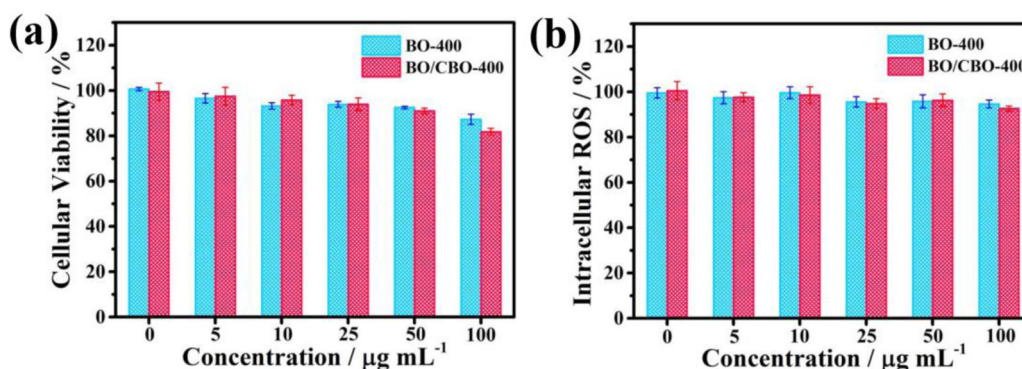


Fig. 8. The cellular viability of A549 cells (a) and the oxidative stress induced by as-prepared samples (b).

photocatalytic reaction (Fig. 6e) [23,29,44]. This Z-scheme heterojunction not only promotes the valid spatial separation of photo-generated carriers, but also achieves the maximum redox capacity for the whole system.

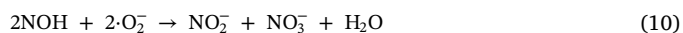
### 3.4. Analysis of the NO adsorption and photocatalytic oxidation

In order to explore the pathways of photocatalytic NO oxidation, *in situ* DRIFTS was employed to dynamically monitor the NO adsorption in the dark and the NO oxidation under visible light on the photocatalyst surface. The absorption peaks in the IR spectra and their corresponding  $\text{NO}_x$  species are listed in Table S2 and Table S3.

During the adsorption stage, the baseline spectrum was recorded before NO and  $\text{O}_2$  were introduced into the reaction chamber. Fig. 7b shows the time-dependent adsorption of NO on the BO/CBO-400 surface. Over time, the absorption bands at  $1018\text{ cm}^{-1}$ ,  $1173\text{ cm}^{-1}$  and  $1440\text{ cm}^{-1}$  are assigned to monodentate, chelating and bridging nitrite, respectively [49–51]. The bands at  $1262\text{ cm}^{-1}$ ,  $1508\text{ cm}^{-1}$  and  $1645\text{ cm}^{-1}$  belong to the bidentate, monodentate and bridging nitrate [51,52]. In addition, NO can be easily oxidized by  $\text{O}_2$  to form  $\text{NO}_2$  ( $1593\text{ cm}^{-1}$ ) (Eq 2) [53], an undesirable toxic intermediate. The detected  $\text{NO}^+$  ( $2150\text{ cm}^{-1}$ ) is produced via the disproportionation of  $\text{NO}_2$  (Eq 3), or NO losing electrons [51,54]. NO can react with hydroxyl groups (broad  $3400\text{ cm}^{-1}$ ) to generate NOH ( $1083\text{ cm}^{-1}$ ) and  $\text{NO}^-$  2 (Eq 4) [47,52]. Compared with the bands in the case of BO-400 (Fig. 7a and Table S2), the emergence of new absorption bands for BO/CBO-400 indicates that the construction of heterojunction facilitates the adsorption and activation of NO, which is beneficial for the photocatalytic removal of NO.

During the photocatalytic stage, the time-dependent evolution of the intermediates and products was recorded. Obviously, new absorption bands at  $1270\text{ cm}^{-1}$ ,  $1487\text{ cm}^{-1}$  and  $1639\text{ cm}^{-1}$  were detected (see Fig. 7d), suggesting the generation of monodentate and bridging nitrate [50,51,55]. The band at  $1015\text{ cm}^{-1}$  is attributed to the monodentate nitrite [49]. It is worth noting that the  $\text{NO}^+$  ( $2150\text{ cm}^{-1}$ ) adsorbed on the BO/CBO-400 was consumed. Compared with that in the dark, the intensity of  $\text{NO}^+$  absorption band ( $2141\text{ cm}^{-1}$ ) increases (Fig. 7c), implying  $\text{NO}^+$  was continuously generated on the surface of BO-400. The absorption peaks of  $\text{NO}_2$  ( $1520\text{ cm}^{-1}$ ) and  $\text{N}_2\text{O}_4$  ( $1685\text{ cm}^{-1}$ ) were not detected on the BO/CBO-400 while those peaks were detected over BO-400, indicating that the generation of toxic intermediates were suppressed in the case of BO/CBO-400 [51].

Moreover, the normalization method is adopted to describe the changes in the content of nitrogen oxides (Fig. S14). The highest nitrate content and the absence of toxic intermediates in BO/CBO-400 indicate that it can selectively convert NO, adsorbed species and intermediates into nitrate through active oxygen species under visible light irradiation. In addition, the monodentate nitrate accounts for the largest proportion of the generated nitrate species, implying that monodentate nitrate is the most stable on the surface of BO/CBO-400.



### 3.5. Cytotoxicity

Considering the practical application of photocatalytic materials in air purification, the toxicity of BO-400 and BO/CBO-400 was evaluated by *in vitro* models. The A549 cells were exposed to different concentrations (from 0 to  $100\text{ }\mu\text{g mL}^{-1}$ ) of photocatalysts. The toxicity of the photocatalyst was evaluated by the survival rate of the cells after exposure. Fig. 8a shows the relationship between cell viability and catalyst concentration. The viability of A549 cells decreased slightly with the enhancement of BO/CBO-400 concentration. Nevertheless, the cellular viability is still higher than 80 %, even at high concentration of  $100\text{ }\mu\text{g mL}^{-1}$ . The toxicity of photocatalysts to A549 cells has also been studied in previous articles. As FeOOH concentration increased from  $0.5\text{--}200\text{ }\mu\text{g mL}^{-1}$ , cell viability decreased to 63 %. However, the CQD/FeOOH composite shows good biocompatibility [56]. Huang et al. reported that cell viability was inhibited by 50 % at  $\text{TiO}_2$  concentration of  $100\text{ }\mu\text{g mL}^{-1}$ , while  $\text{TiO}_2/\text{g-C}_3\text{N}_4$  was almost not toxic to A549 cells [57]. Compared with other photocatalysts, the samples in this study also exhibit good biosecurity. On the other hand, when cells are exposed to external stimuli, reactive oxygen species (ROS) in the cells are produced in large quantities to form oxidative stress [33,34]. This is an important factor leading to apoptosis. Therefore, intracellular ROS are also detected, as shown in Fig. 8b. The results shows that intracellular ROS are hardly changed, indicating that the as-prepared photocatalysts did not induce any oxidative stress. These results show that the prepared photocatalytic materials exhibit very low cytotoxicity. Hence, BO/CBO-400 composite with excellent photocatalytic activity and biocompatibility meets a wide range of applications.

## 4. Conclusion

In summary, we developed an in situ synthesis method to controllably prepare Z-scheme  $\alpha\text{-Bi}_2\text{O}_3/\text{CuBi}_2\text{O}_4$  heterojunction which exhibits dramatically increased photocatalytic activity in terms of NO elimination under visible light irradiation. The high photocatalytic activity of  $\alpha\text{-Bi}_2\text{O}_3/\text{CuBi}_2\text{O}_4$  is attributed to the effective separation and transfer of photogenerated carriers at the intimate interface. The Z-scheme heterojunction can guarantee the strong redox capacity of the photogenerated carriers in the system. The BO/CBO heterojunction is not only conducive to the adsorption and activation of NO on the catalyst surface, but also suppress the generation of the toxic intermediates ( $\text{NO}_2$  and  $\text{N}_2\text{O}_4$ ) to promote the conversion of NO to  $\text{NO}_3^-$  during the photocatalytic process. In addition, the BO/CBO composite displays good biocompatibility, which is critical for practical application of photocatalyst. This study offers a feasible strategy to fabricate Z-scheme heterojunction with strong redox capacity, enhanced separation efficiency of carriers and high selectivity for nitrate generation.

## 5. Credit author statement

**Qian Chen:** Conceptualization, Investigation, Writing - original draft, Methodology, Visualization. **Huimin Long:** Investigation, Data curation, Visualization. **Meijuan Chen:** Resources, Validation. **Yongfang Rao:** Project administration, Supervision, Validation, Writing - review & editing. **Xinwei Li:** DFT calculation. **Yu Huang:** Project administration.

## 6. Declaration of interests

The authors declare that they have no known competing financial interests or personal relationships that could have appeared to influence the work reported in this paper.

## Acknowledgements

This work was financially supported by “Key Laboratory of Aerosol Chemistry and Physics, Institute of Earth Environment, CAS (No. KLACP1701)” and “State Key Laboratory of Loess and Quaternary Geology, Institute of Earth Environment, CAS (No. SKLLQG1516)”.

## Appendix A. Supplementary data

Supplementary material related to this article can be found, in the online version, at doi:<https://doi.org/10.1016/j.apcatb.2020.119008>.

## References

- [1] R.J. Huang, Y. Zhang, C. Bozzetti, K.F. Ho, J.J. Cao, Y. Han, K.R. Daellenbach, J.G. Slowik, S.M. Platt, F. Canonaco, P. Zotter, R. Wolf, S.M. Pieber, E.A. Bruns, M. Crippa, G. Ciarelli, A. Piazzalunga, M. Schwikowski, G. Abbaszade, J. Schnelle-Kreis, R. Zimmermann, Z. An, S. Szidat, U. Baltensperger, I. El Haddad, A.S. Prevot, *Nature* 514 (2014) 218–222.
- [2] L. Zhao, G. Dong, L. Zhang, Y. Lu, Y. Huang, *ACS Appl. Mater. Interfaces* 11 (2019) 10042–10051.
- [3] Y. Peng, W. Si, J. Luo, W. Su, H. Chang, J. Li, J. Hao, J. Crittenden, *Environ. Sci. Technol.* 50 (2016) 6442–6448.
- [4] P. Hu, Z. Huang, X. Gu, F. Xu, J. Gao, Y. Wang, Y. Chen, X. Tang, *Environ. Sci. Technol.* 49 (2015) 7042–7047.
- [5] Q. Jiang, T. Qi, T. Yang, Y. Liu, *Build. Environ.* 158 (2019) 94–103.
- [6] Q. Chen, L. Chen, J. Qi, Y. Tong, Y. Lv, C. Xu, J. Ni, W. Liu, *Chin. Chem. Lett.* 30 (2019) 1214–1218.
- [7] H. Shang, M. Li, H. Li, S. Huang, C. Mao, Z. Ai, L. Zhang, *Environ. Sci. Technol.* 53 (2019) 6444–6453.
- [8] W. He, Y. Sun, G. Jiang, H. Huang, X. Zhang, F. Dong, *Appl. Catal. B: Environ.* 232 (2018) 340–347.
- [9] G. Dong, L. Yang, F. Wang, L. Zang, C. Wang, *ACS Catal.* 6 (2016) 6511–6519.
- [10] H. Wang, W. Zhang, X. Li, J. Li, W. Cen, Q. Li, F. Dong, *Appl. Catal. B: Environ.* 225 (2018) 218–227.
- [11] J. Chen, J. Zhan, Y. Zhang, Y. Tang, *Chin. Chem. Lett.* 30 (2019) 735–738.
- [12] M. Chen, Y. Huang, W. Chu, *Chin. J. Catal.* 40 (2019) 673–680.
- [13] J. Ke, J. Liu, H. Sun, H. Zhang, X. Duan, P. Liang, X. Li, M.O. Tade, S. Liu, S. Wang, *Appl. Catal. B: Environ.* 200 (2017) 47–55.
- [14] H. Lu, Q. Hao, T. Chen, L. Zhang, D. Chen, C. Ma, W. Yao, Y. Zhu, *Appl. Catal. B: Environ.* 237 (2018) 59–67.
- [15] H.-Y. Jiang, J. Liu, K. Cheng, W. Sun, J. Lin, *J. Phys. Chem. C* 117 (2013) 20029–20036.
- [16] D. Chen, S. Wu, J. Fang, S. Lu, G. Zhou, W. Feng, F. Yang, Y. Chen, Z. Fang, *Sep. Purif. Technol.* 193 (2018) 232–241.
- [17] K. Maeda, *ACS Catal.* 3 (2013) 1486–1503.
- [18] J. Hu, D. Chen, Z. Mo, N. Li, Q. Xu, H. Li, J. He, H. Xu, J. Lu, *Angew. Chem. Int. Ed.* 58 (2019) 2073–2077.
- [19] Y. Jia, S. Li, J. Gao, G. Zhu, F. Zhang, X. Shi, Y. Huang, C. Liu, *Appl. Catal. B: Environ.* 240 (2019) 241–252.
- [20] Z. Jiang, W. Wan, H. Li, S. Yuan, H. Zhao, P.K. Wong, *Adv. Mater.* 30 (2018) 1706108.
- [21] J. Low, B. Dai, T. Tong, C. Jiang, J. Yu, *Adv. Mater.* 31 (2019) 1802981.
- [22] H. Li, T. Hu, R. Zhang, J. Liu, W. Hou, *Appl. Catal. B: Environ.* 188 (2016) 313–323.
- [23] Y. Lu, Y. Huang, J.-j. Cao, H. Li, W. Ho, S.C. Lee, *J. Mater. Chem. A Mater. Energy Sustain.* 7 (2019) 15782–15793.
- [24] Z. Wang, Y. Huang, W. Ho, J. Cao, Z. Shen, S.C. Lee, *Appl. Catal. B: Environ.* 199 (2016) 123–133.
- [25] Z. Wang, Y. Huang, L. Chen, M. Chen, J. Cao, W. Ho, S.C. Lee, *J. Mater. Chem. A* 6 (2018) 972–981.
- [26] Y.H. Choi, D.H. Kim, S.H. Hong, *ACS Appl. Mater. Interfaces* 10 (2018) 14901–14913.
- [27] F. Wang, W. Septina, A. Chemseddine, F.F. Abdi, D. Friedrich, P. Bogdanoff, R. van de Krol, S.D. Tilley, S.P. Berglund, *J. Am. Chem. Soc.* 139 (2017) 15094–15103.
- [28] G. Sharma, Z. Zhao, P. Sarker, B.A. Nail, J. Wang, M.N. Huda, F.E. Osterloh, *J. Mater. Chem. A Mater. Energy Sustain.* 4 (2016) 2936–2942.
- [29] X. Yuan, D. Shen, Q. Zhang, H. Zou, Z. Liu, F. Peng, *Chem. Eng. J.* 369 (2019) 292–301.
- [30] L. Wang, G. Yang, D. Wang, C. Lu, W. Guan, Y. Li, J. Deng, J. Crittenden, *Appl. Surf. Sci.* 495 (2019) 143521.
- [31] W. Shi, F. Guo, S. Yuan, *Appl. Catal. B: Environ.* 209 (2017) 720–728.
- [32] N.B. Hartmann, F. Von der Kammer, T. Hofmann, M. Baalousha, S. Otfoellung, A. Baun, *Toxicology* 269 (2010) 190–197.
- [33] K.N. Yu, T.J. Yoon, A. Minai-Tehrani, J.E. Kim, S.J. Park, M.S. Jeong, S.W. Ha, J.K. Lee, J.S. Kim, M.H. Cho, *Toxicol. In Vitro* 27 (2013) 1187–1195.
- [34] J. Li, H. Yang, S. Sha, J. Li, Z. Zhou, Y. Cao, *Ecotoxicol. Environ. Saf.* 186 (2019) 109770.
- [35] M.K. Hossain, G.F. Samu, K. Gandha, S. Santhanagopalan, J.P. Liu, C. Janáky, K. Rajeshwar, *J. Phys. Chem. C* 121 (2017) 8252–8261.
- [36] D.R. Bengt Hallstedt, Ludwig J. Gauckler, *J. Am. Ceram. Soc.* 79 (1996) 353–358.
- [37] B. Shao, X. Liu, Z. Liu, G. Zeng, Q. Liang, C. Liang, Y. Cheng, W. Zhang, Y. Liu, S. Gong, *Chem. Eng. J.* 368 (2019) 730–745.
- [38] F. Guo, W. Shi, H. Wang, H. Huang, Y. Liu, Z. Kang, *Inorg. Chem. Front.* 4 (2017) 1714–1720.
- [39] K.S. Joya, H.J.M. de Groot, *ACS Catal.* 6 (2016) 1768–1771.
- [40] H.-Y. Jiang, P. Li, G. Liu, J. Ye, J. Lin, *J. Mater. Chem. A Mater. Energy Sustain.* 3 (2015) 5119–5125.
- [41] Y. Huang, W. Wang, Q. Zhang, J.J. Cao, R.J. Huang, W. Ho, S.C. Lee, *Sci. Rep.* 6 (2016) 23435.
- [42] Y. Wang, H. Wang, A.R. Woldu, X. Zhang, T. He, *Catal. Today* 335 (2019) 388–394.
- [43] X. Li, Y. Sun, T. Xiong, G. Jiang, Y. Zhang, Z. Wu, F. Dong, *J. Catal.* 352 (2017) 102–112.
- [44] F. Guo, W. Shi, H. Wang, M. Han, W. Guan, H. Huang, Y. Liu, Z. Kang, *J. Hazard. Mater.* 349 (2018) 111–118.
- [45] J. Li, X. Wu, Z. Wan, H. Chen, G. Zhang, *Appl. Catal. B: Environ.* 243 (2019) 667–677.
- [46] J. Ran, W. Guo, H. Wang, B. Zhu, J. Yu, S.Z. Qiao, *Adv. Mater.* 30 (2018) 1800128.
- [47] X. Li, W. Zhang, J. Li, G. Jiang, Y. Zhou, S. Lee, F. Dong, *Appl. Catal. B: Environ.* 241 (2019) 187–195.
- [48] L. Jiang, X. Yuan, G. Zeng, J. Liang, X. Chen, H. Yu, H. Wang, Z. Wu, J. Zhang, T. Xiong, *Appl. Catal. B: Environ.* 227 (2018) 376–385.
- [49] W. Cui, J. Li, F. Dong, Y. Sun, G. Jiang, W. Cen, S.C. Lee, Z. Wu, *Environ. Sci. Technol.* 51 (2017) 10682–10690.
- [50] K. Hadjiivanov, *Langmuir* 18 (2002) 1619–1625.
- [51] K.I. Hadjiivanov, *Catal. Rev.* 42 (2000) 71–144.
- [52] J. Wu, Y. Cheng, *J. Catal.* 237 (2006) 393–404.
- [53] X. Li, W. Zhang, W. Cui, Y. Sun, G. Jiang, Y. Zhang, H. Huang, F. Dong, *Appl. Catal. B: Environ.* 221 (2018) 482–489.
- [54] E.Z.C. Margarita Kantcheva, *J. Phys. Chem. B* 106 (2002) 3941–3949.
- [55] F.E. López-Suárez, M.J. Illán-Gómez, A. Bueno-López, J.A. Anderson, *Appl. Catal. B: Environ.* 104 (2011) 261–267.
- [56] Y. Huang, Y. Gao, Q. Zhang, Y. Zhang, J.-j. Cao, W. Ho, S.C. Lee, *J. Hazard. Mater.* 354 (2018) 54–62.
- [57] Y. Huang, P. Wang, Z. Wang, Y. Rao, J.-j. Cao, S. Pu, W. Ho, S.C. Lee, *Appl. Catal. B: Environ.* 240 (2019) 122–131.